NJC

ROYAL SOCIETY OF CHEMISTRY

PAPER

View Article Online
View Journal

Cite this: DOI: 10.1039/d5nj03310a

Decoupled impact of acidity and mesoporosity on catalyst deactivation during glycerol dehydration over ZSM-5 zeolites

Yonghua Yu,[ab] Jing Niu,[a] Dazhi Zhang,*[a] Shutao Xu,[a] Fang Lu,[a] Jiaxu Liu[c] and Shengjun Huang*[a]

Catalytic glycerol dehydration to acrolein is an attractive value-added route for the reasonable utilization of bio-derived glycerol. ZSM-5 zeolites have been widely investigated in glycerol dehydration due to their initial catalytic performance and environmentally benign nature. However, ZSM-5 zeolite-based catalysts suffer from rapid deactivation. It is known that the acidity and porosity of the ZSM-5 zeolites influence the reaction. However, due to the interdependence and interplay between the acidity and porosity of zeolite, it is challenging to understand their respective roles in this reaction. Herein, the acidity and porosity of ZSM-5 zeolites are decoupled to investigate the separate roles and their interplay in the dehydration of glycerol. It is demonstrated that the accessibility of the acid sites is critical to the catalytic performance of the dehydration of glycerol. In this regard, the activity profile of microporous ZSM-5 zeolites with limited accessibility to the acid sites is characterised by a sharp decline from the beginning of the reaction, despite possessing the highest acid site density. The accessibility of the acid sites can be mitigated with hybrid mesoporosity. As a consequence, the acid sites at the low density level (only *ca.* 7% of the reference value of microporous ZSM-5) enable smooth running and high conversion (~95%) of the reaction within 10 hours on the hierarchical ZSM-5 zeolites. However, the fast deactivation remains a challenge for the hierarchical ZSM-5 zeolites after the initial steady dehydration of glycerol. It is worth noting that the deactivation of the zeolite is not solely due to the blockage by carbonaceous species. Along with the progress of the dehydration reaction, the accessibility of the acid sites re-emerges as the factor responsible for the decline of the activity over the hierarchical zeolite, which stems from blockage by polyglycols due to the thermal or acid-driven intermolecular dehydrations. These observations enrich our fundamental understanding of the deactivation of the glycerol dehydration reaction and are informative for the emergence of refinement strategies to mitigate the deactivation bottlenecks.

Received 16th August 2025,
Accepted 28th October 2025

DOI: 10.1039/d5nj03310a

rsc.li/njc

Introduction

Biodiesel is an eco-friendly and sustainable form of energy as it is naturally sourced from vegetable and animal oils.[1–3] Glycerol is produced as a by-product of biodiesel manufacturing, with an approximate 10 wt% output of the total biodiesel production.[4,5] Growing demand for biodiesel will thus lead to the oversupply of glycerol. The effective utilization of glycerol is crucial to improve the economic feasibility and sustainability of biodiesel production. Glycerol can be converted into high-value-added chemicals *via* hydrogenolysis,[6–8] oxidation,[9–11] dehydration, *etc.*[12–15] Particularly, acid-catalyzed dehydration of glycerol to synthesize acrolein is an attractive transformation route.

The dehydration of glycerol is an acid-catalyzed reaction that can be propelled by liquid or solid acid catalysts.[16–18] Several solid acid catalysts have been applied in glycerol dehydration, including heteropoly acids,[19–21] mixed metal oxides,[22,23] and zeolites.[14,24–26] Among them, zeolites serve as promising catalysts for the dehydration of glycerol due to their operational advantages. In particular, ZSM-5 zeolites have been extensively used in this dehydration reaction.[27–31] Versatile ZSM-5 zeolites with different acidities and porosities have been investigated in this reaction; however, their interdependence and complex interplays make understanding the roles of acidities and porosities difficult. On the one hand, the impact of the acidity of

[a] *Dalian Institute of Chemical Physics, Chinese Academy of Sciences, Dalian, 116023, China. E-mail: huangsj@dicp.ac.cn, dzh_zhang3@dicp.ac.cn*
[b] *University of Chinese Academy of Sciences, Beijing, 100049, China*
[c] *School of Chemical Engineering, Dalian University of Technology, Dalian, 116024, China*

the zeolite on the reaction has been emphasized. For instance, it has been found that siliceous H-ZSM-5 (SiO_2/Al_2O_3 = 150) displays higher activity and catalytic stability than its aluminum-rich H-ZSM-5 counterpart (SiO_2/Al_2O_3 = 30) in the dehydration of glycerol.[32] The selectivity for acrolein formation can be linked to the strength of the zeolite acidity.[33] On the other hand, the critical roles of the porosity have been highlighted in this reaction. In the catalytic dehydration of glycerol by zeolite, the main challenge is the fast deactivation of the catalyst, which has been solely attributed to pore blockage by carbonaceous species. To cope with the deactivation, various strategies have been developed. In particular, the introduction of mesoporosity has been demonstrated to enhance the target selectivity and the reaction stability. For example, the hierarchical ZSM-5 zeolites improved the catalytic stability and selectivity owing to the reduction of diffusion limitations and the enhanced accessibility of acid sites.[31,34–36] However, the ZSM-5 zeolites still suffer from rapid deactivation in the dehydration of glycerol, regardless of the tailoring in acidities and porosities. In particular, the interdependence and interplay between the acidity and porosity complicate the understanding of their roles. From a more delicate perspective, it is more desirable to distinguish the respective impact of the acidities and porosities on controlled zeolite systems; that is, a controlled porosity with a gradient of acidities or the controlled integration of porosity and acidity.

In this work, the acidities and porosities of ZSM-5 zeolites are decoupled to demonstrate their impacts on the dehydration of glycerol. The initial comparisons, based on the microporous ZSM-5 zeolite (SiO_2/Al_2O_3 = 25, 70, 500) ratios, display the experimental scenarios of fast deactivation, which is characteristic of the sharp declining activity profile from the beginning of the reaction, despite the highest acid-site density. Apparently, the microporosity limits the accessibility of the acid sites to the glycerol molecules. In order to conduct a robust discussion, hierarchical ZSM-5 zeolites, bearing controlled mesoporosity with a gradient of acidities, were constructed for the reaction. With the hybrid mesoporosity, acid sites at low-density levels enable the smooth running and high conversion of the reaction for on the order of 10 hours. In this regard, the accessibility of the acids is a priority for the dehydration of glycerol. Nevertheless, after the initial steady stage, the hierarchical ZSM-5 zeolites still face the challenges of deactivation, and introducing high levels of acid site density barely benefits the dehydration of glycerol. On the other hand, the enhanced acid site density leads to the structural sophistication of carbonaceous species to poly-aromatics. It is worth noting that the blockage of acid sites by carbonaceous species is not the sole reason for the deactivation of the zeolite catalysts. Along with the progress of the dehydration reaction, the accessibility of the acid sites re-emerges as the factor responsible for the decline of the activity over the hierarchical zeolite, which stems from blockage by polyglycols formed from thermal or acid-driven intermolecular dehydrations. The results update our understanding of the deactivation from a sole pathway to dual deactivation pathways: one from carbonaceous species and a second from polyglycols.

Experimental section

Pristine material

The commercially available protonic forms of the ZSM-5 zeolites were purchased from Catalyst Plant of Nankai University and used without further purification. These ZSM-5 zeolites, with SiO_2/Al_2O_3 ratios of 25, 70 and 500, were noted as Z25, Z70 and Z500, respectively.

Alkaline treatment

The alkaline treatment was performed as follows: the parent Z500 was treated with alkaline in a mixed aqueous solution of 0.2 M NaOH and $Al(NO_3)_3$ with specific concentrations (0.003 M, 0.005 M and 0.015 M) at 65 °C for 30 min. The suspension was filtered, washed with deionized water, and dried at 100 °C overnight. Then, the sample was washed in 0.1 M HNO_3 solution at 60 °C for 5 h prior to NH_4^+-exchange. The final protonic-form zeolite was denoted as AT(x)-Z500, where x stands for the concentration of aluminum nitrate in mol L^{-1} used in the NaOH solution.

Comparative alkaline treatment of Z70

The parent Z70 was treated in aqueous 0.2 M NaOH solution at 65 °C for 30 min. The suspension was filtered, washed with deionized water, and dried at 100 °C overnight. Finally, the zeolite was converted into the protonic form *via* three successive exchanges in 0.8 M NH_4Cl followed by calcination at 550 °C for 3 h. The final protonic-form zeolite was denoted as AT-Z70.

Characterization

The crystalline structure of the zeolites was characterized by the powder X-ray diffraction (XRD) analysis with an X'pert Pro-1 Diffractometer with Cu-Kα radiation. The N_2 adsorption measurements were carried out at liquid-nitrogen temperature with a Micromeritics ASAP 2460 instrument after degassing at 350 °C for 10 h under evacuation. The specific surface area of the samples was determined by using the Brunauer–Emmett–Teller (BET) equation. The total pore volumes were evaluated from the volume adsorbed at P/P_0 = 0.99, and the micropore area and volume were determined by the t-plot method. Field emission scanning electron microscope (FESEM) observations were obtained with a JEOL JSM-7800F microscope, and high-resolution transmission electron microscopy (HRTEM) characterizations were performed with a JEOL JEM-2100 microscope.

The NH_3-TPD experiments were carried out with a Micromeritics AutoChem 2920 instrument in the range of 100–600 °C, and the desorbed ammonia was monitored with a gas chromatograph fitted with a TCD detector. The coke species on the spent catalysts were extracted by a dissolution-extraction method, and their composition and identification were determined by gas chromatograph-mass spectrometry (GC-MS). Typically, 15.0 mg of spent catalyst was first dissolved in 2 mL 40% HF solution and extracted with CH_2Cl_2. Then, the CH_2Cl_2-extracted organic compounds were analyzed by a GC-MS (7890A/5975C, Agilent) equipped with a HP-5 capillary column and a flame ionization detector. The weight loss of

the spent ZSM-5 zeolite catalysts was analyzed by using a PerkinElmer Thermogravimetric Analyzer TGA4000 in the temperature range of 30 °C to 800 °C under an air atmosphere at a ramp rate of 10 °C min^{-1}. Solid-state ^{13}C MAS-NMR spectra of the spent MFI zeolites were recorded with a Bruker Avance III 500 MHz spectrometer equipped with a 4.0 mm probe and operated with a rotor-spinning rate of 12 kHz. The parameters for measurements are as follows: operating frequency of 83 kHz, a pulse width of 4.7 μs, and a contact time of 3000 μs.

Catalyst evaluation

The gas-phase glycerol dehydration reaction was evaluated in a stainless steel fixed-bed reactor at atmospheric pressure. Before the tests, the catalyst (1.0 g, 20–40 mesh) was placed in the fixed-bed reactor and treated with N_2 at 450 °C for 2 h. After being cooled to the desired reaction temperature, 20 wt% glycerol aqueous solution was fed into the reactor with a N_2 flow of 20 mL min^{-1}. The reaction was performed at 320 °C, and the products were collected with a cold trap and then analyzed by an Agilent 7890B gas chromatograph equipped with a cold trap and then with an Agilent 7890B gas chromatograph equipped with a HP-FFAP capillary column (30 m × 0.32 mm × 0.25 mm) and a flame ionization detector. The glycerol conversion (X) and the product selectivity (S) were calculated from the following equations:

$$X = \frac{n_{in} - n_{out}}{n_{in}} \times 100\%$$

$$S = \frac{n_i}{n_{in} - n_{out}} \times 100\%$$

where n_{in} and n_{out} represent the molar amount of glycerol at the inlet and outlet of the reactor, respectively, and n_i is the molar amount of acrolein.

Results and discussion

Catalytic results

The primary performance of parent microporous ZSM-5 zeolites with different SiO_2/Al_2O_3 ratios is compared in Fig. 1. The Al-rich zeolite Z25 gives the lowest initial conversion of glycerol (47%) and exhibits a steady decline in activity during the reaction. Although the siliceous counterparts of Z70 and Z500 display higher initial conversion levels (*ca.* 85%), their stabilities are characterized by a sharp decline to *ca.* 40% within 12 hours. Based on the NH_3-TPD profiles of these microporous ZSM-5 zeolites, the density of acid sites for Z25 is set as 100% reference, and the relative densities of Z70 and Z500 are 34% and 5%, respectively. Although NH_3-TPD cannot differentiate

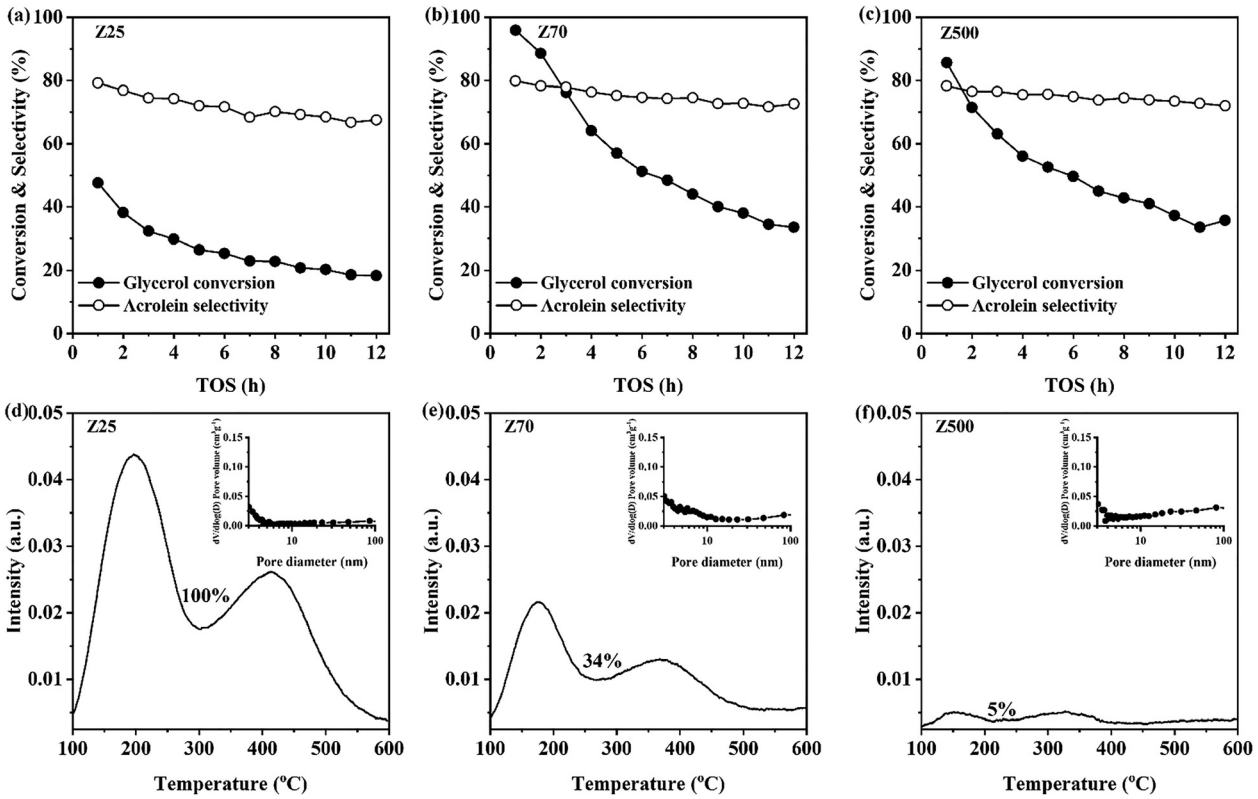

Fig. 1 (a)–(c) Glycerol conversion and acrolein selectivity over the microporous ZSM-5 zeolites with different SiO_2/Al_2O_3 ratios. (d)–(f) The NH_3-TPD profiles of the microporous ZSM-5 zeolites and BJH pore size distribution curves derived from the adsorption branches of the isotherms (inset). Reaction conditions: 320 °C, atmospheric pressure, and WHSV = 1.25 h^{-1}. (Note: the density of acid sites for Z25 is set as 100% reference.)

the type of acidity (Brønsted or Lewis type), such significant differences still confirm the poor level of acidity over the Z500. It seems that most of the acid sites within microporous Z25 barely contribute to the dehydration reaction, and higher SiO_2/Al_2O_3 ratios of the zeolite benefit the dehydration to acrolein. However, it should be noted that the aforementioned observations are obtained over these deactivation-ongoing ZSM-5 zeolites. It is more reasonable to make the comparison under relatively steady situations.

Porosity and acidity are typically two impacting factors for the tailoring of the zeolite catalyst for the acid-catalyzed dehydration of glycerol. However, the alterations in porosity and acidity are often concomitant, which complicates the differentiation of their individual contributions to the reaction. Due to its poor level of acidity, the highly siliceous Z500 is used to demonstrate the roles of porosity. The microporous Z500 is turned into its hierarchical counterparts by alkaline treatment in the presence of soluble Al agents. As shown in Fig. 2, it was found that the initial activity and catalytic stability of the catalysts can be enhanced upon the introduction of mesoporosity into the Z500 zeolites (Fig. 2e and f). The glycerol conversion over AT(0.003)-Z500 reaches 95% and the deactivation profile is flattened, with the conversion remaining around 80% during the time-on-stream of 12 hours. A further enhanced stability is observed on the AT(0.005)-Z500, the activity profile of which is relatively smooth and remains above 95% for up to 12 hours. The NH_3-TPD profiles of AT(0.003)-Z500 and AT(0.005)-Z500 still prove their poor levels of acidity despite their slight enhancement to 7% and 10%, respectively. Therefore, the introduced mesoporosity outweighs the acidity in this dehydration reaction. In other words, the accessibility of the acid sites overtakes their nature and density. As a supportive result, the augmentation of acid site densities over the AT(0.015)-Z500 gives a similar catalytic performance to that of AT(0.005)-Z500 (Fig. S1). The introduction of mesoporosity into the relatively Al-rich zeolite of Z70 also has analogous consequences on the reaction. Despite bearing almost quadruple acid site density, the hierarchical AT-Z70 gives an activity profile that is highly similar to that of AT(0.005)-Z500 (Fig. 3). Under the condition that the accessibility of the acid sites is addressed, enhancement of the acid site density does not definitely translate to enhanced catalytic performance, which indicates a saturated level of acid site density for glycerol dehydration. It also implies an alternative perspective on understanding the roles of acid sites in the reaction. In particular, the association of acid sites with the challenging issue of catalytic stability has been practically overlooked, and this aspect deserves an assessment.

On the other hand, the selectivity for the formation of acrolein of all the microporous ZSM-5 zeolites is about 80%. Upon the introduction of mesoporosity into the Z500 zeolites, the selectivity to acrolein was also around 80% and was not

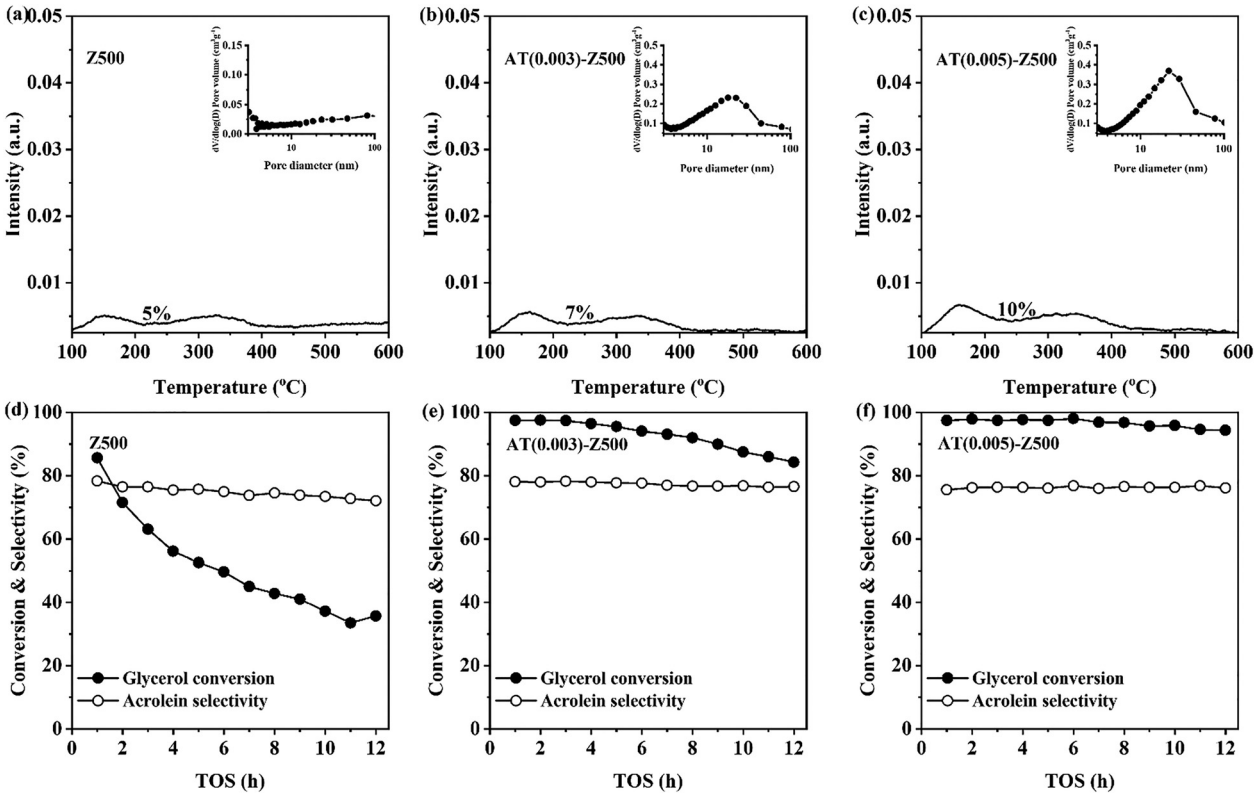

Fig. 2 (a)–(c) NH_3-TPD profiles of AT(0.003)-Z500 and AT(0.005)-Z500, and the BJH pore size distribution curves derived from the adsorption branches of the isotherms (inset). (d)–(f) Glycerol conversion and acrolein selectivity over the Z500, AT(0.003)-Z500 and AT(0.005)-Z500. Reaction conditions: 320 °C, atmospheric pressure, WHSV = 1.25 h^{-1}. (Note: the density of acid sites for Z25 is set as 100% reference.)

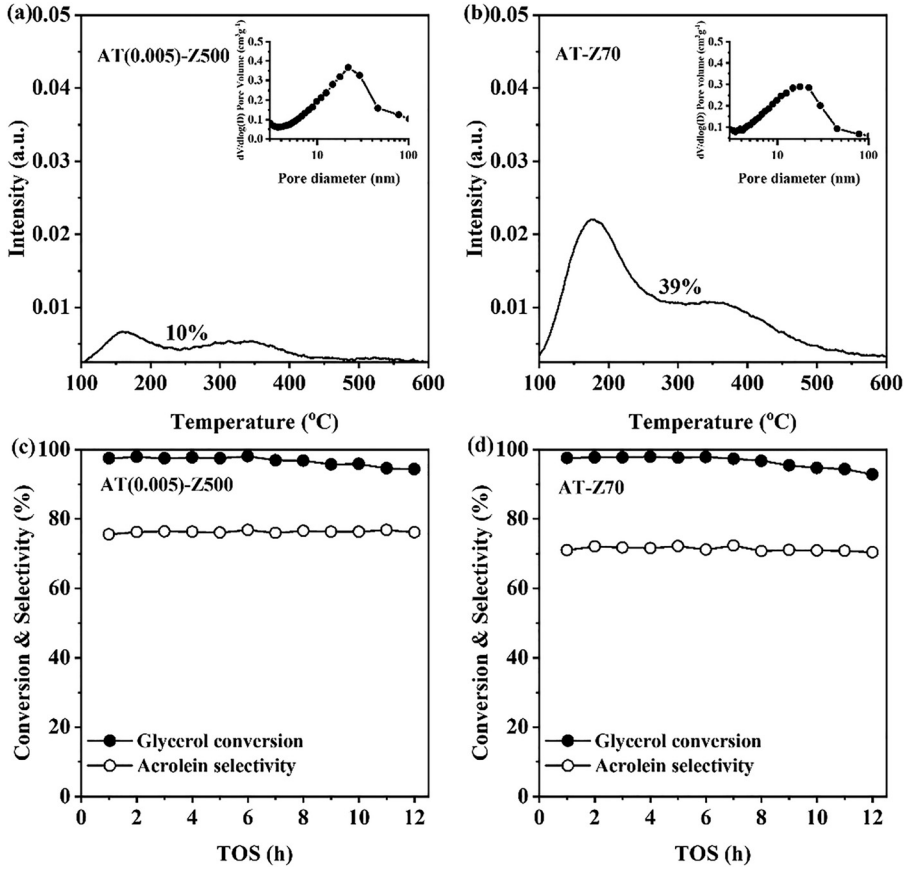

Fig. 3 (a) and (b) NH_3-TPD profiles of AT(0.005)-Z500 and AT-Z70 and the BJH pore size distribution curves derived from the adsorption branches of the isotherms (inset). (c) and (d) Glycerol conversion and acrolein selectivity over the hierarchical AT(0.005)-Z500 and AT-Z70. Reaction conditions: 320 °C, atmospheric pressure, and WHSV = 1.25 h^{-1}. (Note: the density of acid sites for Z25 is set as 100% reference.)

significantly affected by the improvement of catalytic stability. However, the selectivity to acrolein is reduced to approximately 70% with a higher proportion of the by-product acetaldehyde for AT-Z70, which is due to the enhanced retro-aldol reaction of acrolein or the 3-hydroxypropionaldehyde intermediate.[33,37]

Characterization of controlled catalysts

Characterization of controlled microporous zeolites. As shown in the XRD patterns (Fig. 4a), the pristine ZSM-5 zeolites with various SiO_2/Al_2O_3 ratios show five characteristic diffraction peaks of a typical MFI topological structure (2θ = 7.9°, 8.9°, 23.1°, 23.3°, and 24.4°). The isotherms of pristine ZSM-5 zeolites measured by N_2 adsorption are typical of type I, and the derived PSD curves show the absence of a mesopore distribution, confirming their microporous nature in the porosity (Fig. 4b and c). The texture properties listed in Table S1 show that the pristine microporous ZSM-5 zeolites possess comparable specific surface area (S_{BET}, 403–419 m^2 g^{-1}) and

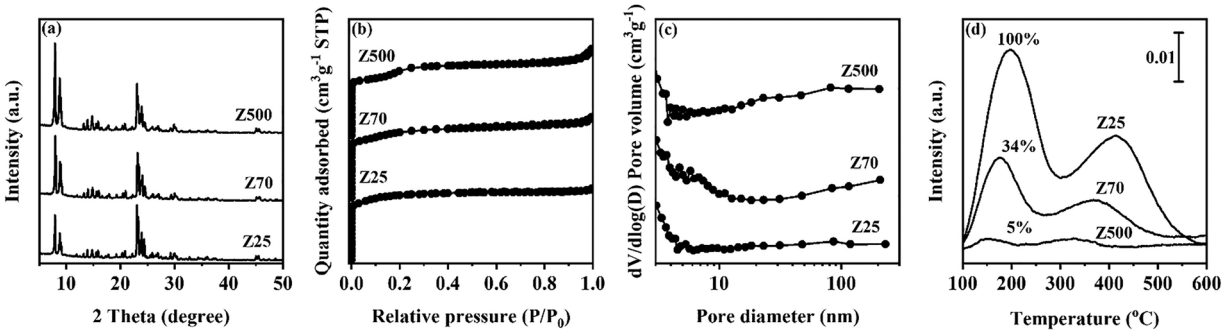

Fig. 4 Physicochemical properties of the pristine microporous ZSM-5 zeolites with various SiO_2/Al_2O_3 ratios. XRD patterns (a), N_2 adsorption–desorption isotherms (b), BJH pore size distribution curves derived from the adsorption of the isotherms (c), and NH_3-TPD profiles (d). (Note: the density of acid sites for Z25 is set as 100% reference.)

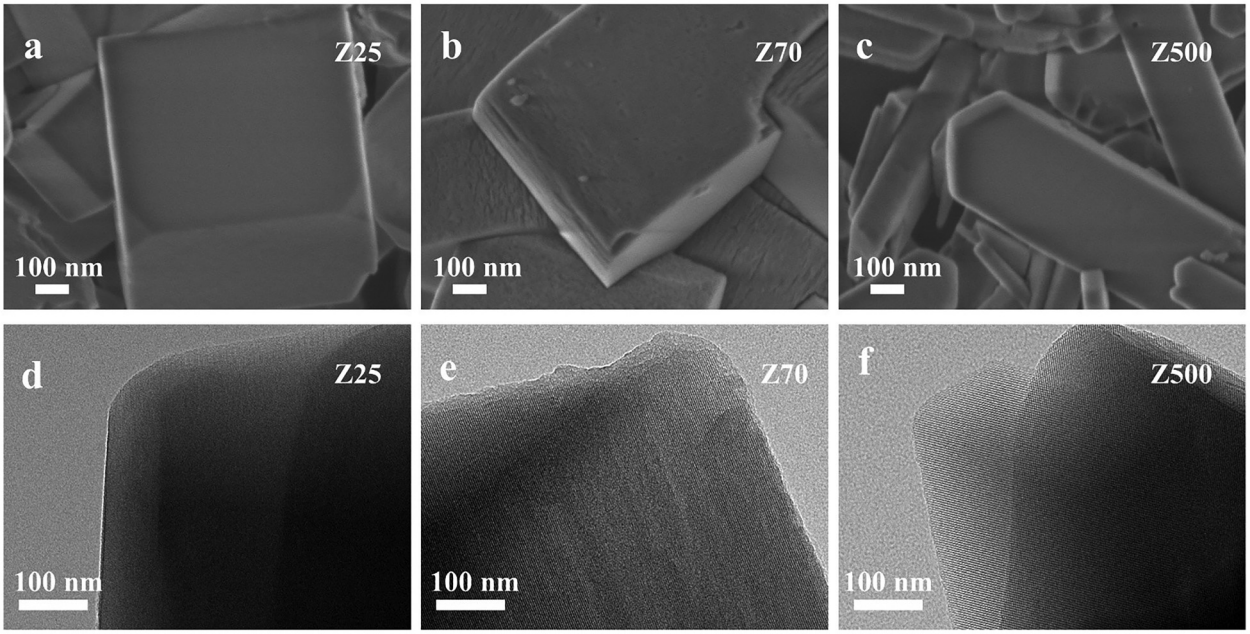

Fig. 5 SEM and TEM images of the pristine microporous ZSM-5 zeolites with the various SiO_2/Al_2O_3 ratios. (a) and (d) Z25, (b) and (e) Z70, and (c) and (f) 500.

microporous volume (V_{micro}, 0.17–0.18 $cm^3\ g^{-1}$). The acidic properties were examined by NH_3-TPD and the results are shown in Fig. 4d. The reduction of acidity density is observed along with the enhancements in the SiO_2/Al_2O_3 ratio. The SEM images in Fig. 5a–c show that pristine ZSM-5 zeolites exhibit hexagonal columnar crystal morphology with a smooth external surface. The TEM images exhibit typical lattice structures with homogeneous contrast (Fig. 5d–f).

Characterization of controlled hierarchical zeolites. After alkaline treatment in the presence of soluble aluminum salt ($Al(NO_3)_3$), all the diffraction peaks of the MFI topology are well preserved (Fig. 6a). The isotherms of AT(0.003)-Z500 and AT(0.005)-Z500 are similar, and give combined type I and type IV, with evident hysteresis loops in the relative pressure range of P/P_0 = 0.4–1.0, which is indicative of the coexistence of the original micropores and the newly formed mesopores in the resulting hierarchical zeolites (Fig. 6b). Moreover, the derived PSD curves of these two hierarchical zeolites display evident mesopore distribution centered at around 20 nm. Accordingly, AT(0.003)-Z500 and AT(0.005)-Z500 achieve similar mesoporous (S_{meso}, 92 $m^2\ g^{-1}$, and 98 $m^2\ g^{-1}$) and microporous (S_{micro}, 351 $m^2\ g^{-1}$, and 359 $m^2\ g^{-1}$) surface areas. As shown in Fig. 6d, the analogous NH_3-TPD profiles of AT(0.003)-Z500 and AT(0.005)-Z500 indicate slight enhancements of their relative acidity densities to 7% and 10%, respectively. In comparison to the smooth surface of the pristine zeolites Z500, dense pore openings throughout the external surface are observed over the AT(0.003)-Z500 and AT(0.005)-Z500, whereas the hexagonal columnar crystal morphology is well preserved (Fig. 7a and b). The TEM images show alternately bright and dark contrast areas (Fig. 7c and d). The light patches are associated with the presence of mesopores in the obtained hierarchical zeolites. These characterization results indicate comparable mesoporosities with poor yet comparable acidity densities.

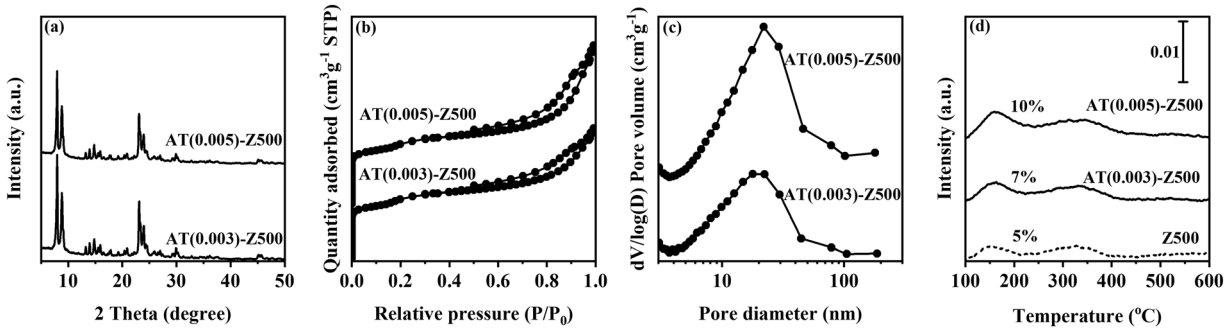

Fig. 6 Physicochemical properties of the hierarchical AT(0.003)-Z500 and AT(0.005)-Z500. XRD patterns (a), N_2 adsorption–desorption isotherms (b), BJH pore size distribution curves derived from the adsorption of the isotherms (c), and NH_3-TPD profiles (d). (Note: the density of acid sites for Z25 is set as 100% reference.)

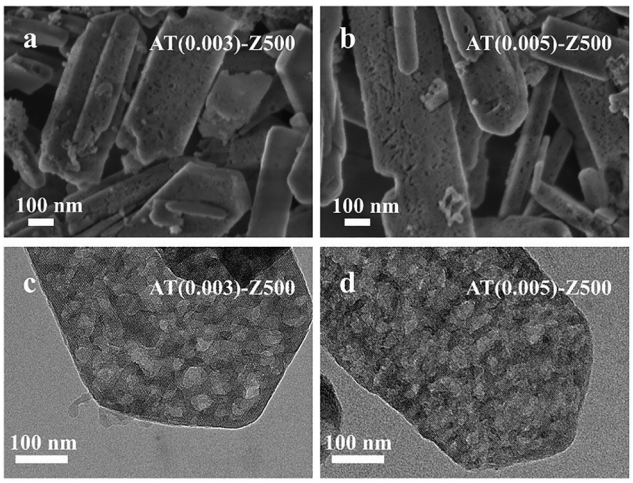

Fig. 7 SEM and TEM images of hierarchical AT(0.003)-Z500 and AT(0.005)-Z500. (a) and (c) AT(0.003)-Z500, (b) and (d) AT(0.005)-Z5.

Another situation was also examined in which samples had comparable mesoporosity alongside a notably higher acidity density. As shown in Fig. S2, AT-Z70 contains comparable mesoporous (S_{meso}, 115 m^2 g^{-1}) and microporous (S_{micro}, 328 m^2 g^{-1}) surface areas, and displays a distinct mesopore distribution centered at 20 nm. The NH_3-TPD profile of AT-Z70 indicates a notable enhancement of its relative acidity density to 39%. The SEM and TEM images also evidence the abundance of intracrystalline mesopores (Fig. S3).

Discussion

As an acid-catalyzed reaction, the nature of the acid sites, including their type, strength, density, and proximity, always has priority in the discussion. However, poor initial conversion and steadily declining catalytic stability are observed over the ZSM-5 zeolites with a wide range of SiO_2/Al_2O_3 ratios from 25 to 500. Given the molecular size of glycerol (0.5 nm), such phenomena indicate the diffusion and accessible limitation imposed by the micropores of the ZSM-5 zeolites (0.55 × 0.51 nm, 0.56 × 0.53 nm), which accounts for the poor response of catalytic performance to the alterations in the acidity within the pure microporous ZSM-5 counterparts. It is well known that mesoporosity is a solution to these limitations.[38] For instance, the siliceous hierarchical AT(0.003)-Z500 enables an initial conversion of 95% and a notably flattened deactivation profile. Such improvement is achieved solely upon the introduction of mesoporosity, in that its acidity density remains at the poor level of 7% (5% for Z500 and 100% for Z25, respectively). However, even in the presence of mesoporous architecture, the catalytic stability of the hierarchical zeolite catalysts still cannot be fully addressed by the enhanced acid density. After 12 h of reaction, the glycerol conversion decreased from 98% to 94% over AT(0.005)-Z500, with relative acidity density around 7%, and from 98% to 93% over AT-Z70, with relative acidity density around 39%. Although the presence of a mesoporous architecture can mitigate the issues of diffusion and accessibility, the dehydration of glycerol still suffers from deactivation. In other words, the acid sites not only serve as the reactive sites for the dehydration but are also associated with the inevitable serious carbonaceous species formation.

The analysis of the deposited carbonaceous species on the spent catalysts provides a probe to investigate such associations. As shown in Fig. 8a, thermogravimetric analysis (TGA) of the spent microporous ZSM-5 zeolites indicates a weight loss of 6.9% over Z25, 9.6% over Z70, and 3.7% over Z500, respectively. After 12 hours of time-on-stream, the spent Z25 shows barely any porosity, which indicates a severe blockage or coverage of micropores by carbonaceous species. Compared to the spent Z25, part of the microporosity can still be observed on the spent Z70 and Z500, which indicates the less severe blockage or coverage of the micropores of these two samples (see Fig. S4 and Table S2). Given the comparable weight loss but different acid site densities of the spent catalysts, this phenomenon

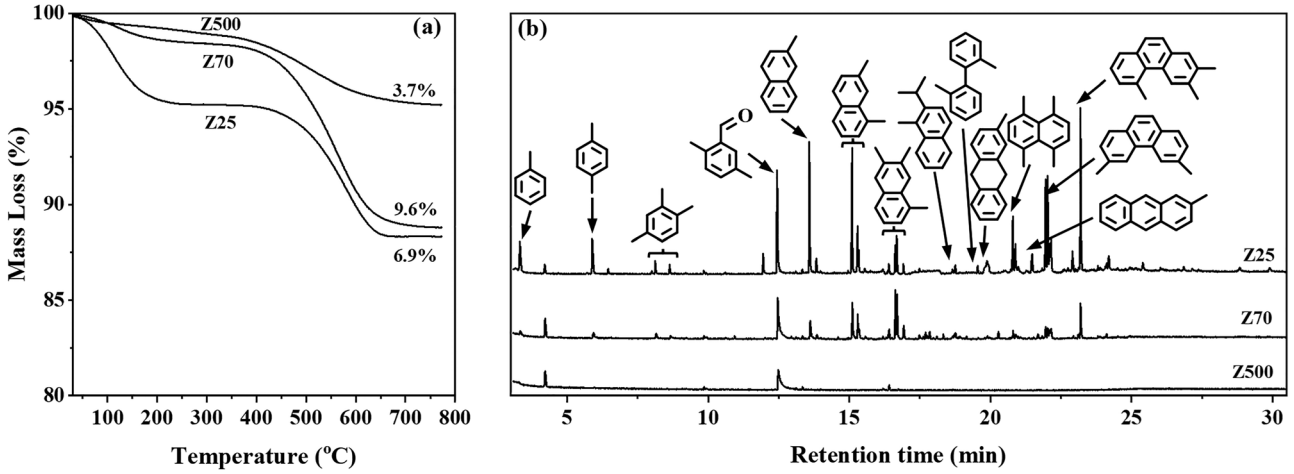

Fig. 8 Characterizations of spent microporous ZSM-5 zeolites. (a) Thermal gravimetric analysis (TGA) and (b) GC-MS chromatograms of the carbonaceous species.

implies that different types of carbonaceous species are generated as a function of the acid site density over the microporous zeolites. The carbonaceous species deposited on the spent microporous zeolite catalysts were extracted by a dissolution-extraction method and subjected to GC-MS analysis. As shown in Fig. 8b, the carbonaceous species can be categorized into three types: monocyclic aromatics (toluene, xylene, trimethylbenzene and 2,5-dimethylbenzaldehyde), bicyclic aromatics (1-methylnaphthalene, 1,7-dimethylnaphthalene, 1,6,7-trimethylnaphthalene and 1,4,5,8-tetramethylnaphthalene), and tricyclic aromatics (2-methylanthracene, 3,6-dimethylphenanthrene and 2,3,5-trimethylphenanthrene). According to the relative intensity of the chromatogram peaks in the GC-MS, the bicyclic aromatics and tricyclic aromatics are the major carbonaceous species deposited on the microporous Z25. In the case of the spent Z70, the bicyclic aromatics are still the major deposited carbonaceous species, whereas the fraction of tricyclic aromatics is significantly reduced. Instead of the bicyclic and tricyclic aromatics, the deposited carbonaceous species on the spent Z500 is the monocyclic aromatic of methyl-substituted benzene. It is evident that the reduction in acid site density suppresses the formation of carbonaceous species and impedes their transitions to the polycyclic species.

Analogous association between the acid site density and types of carbonaceous species is also observed over the hierarchical zeolite catalysts. As shown in Fig. 9a, thermogravimetric analysis (TGA) of the spent hierarchical ZSM-5 zeolites indicates a weight loss of 7.6% over AT(0.003)-Z500, 9.7% over AT(0.005)-Z500, and 14.8% over AT-Z70. The changes in the weight loss on the spent hierarchical ZSM-5 zeolites exhibit a dependence on the acid site density. A structural change in the deposited carbonaceous species as a function of the acid site density is also observed. As shown in the chromatogram presented in Fig. 9b, the major carbonaceous specie over the AT(0.003)-Z500 and AT(0.005)-Z500 is 2,5-dimethylbenzaldehyde, whereas bicyclic and tricyclic aromatics are also observed as the major carbonaceous species over the AT-Z70.

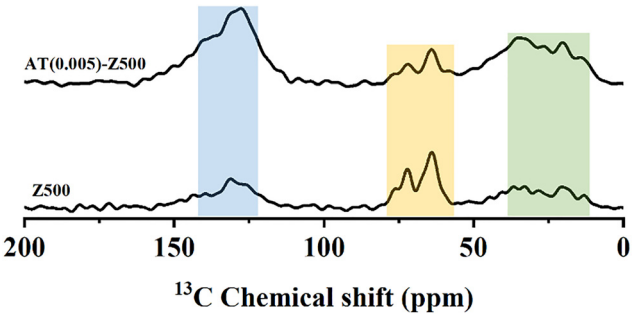

Fig. 10 ^{13}C CP-MAS NMR spectra of the spent Z500 and AT(0.005)-Z500 after 12 h of reaction.

Such structural sophistication of carbonaceous species is also parallel to the enhancement in their relative acid site density (7% for AT(0.003)-Z500, 10% for AT(0.005)-Z500, and 39% for AT-Z70). The slightly higher acid site density level over fresh hierarchical zeolites (7% and 10% for AT(0.003)-Z500 and AT(0.005)-Z500, respectively, *vs.* 5% for Z500) enables a remarkably higher and more stable catalytic performance than their microporous Z500 counterpart in the dehydration of glycerol, which indeed demonstrates the critical roles of mesoporosities from the viewpoint of accessibility of acid sites in the catalytic dehydration of glycerol. It should be noted that these hierarchical zeolite catalysts still suffer from the steady decline in the catalytic performance, despite the presence of mesoporosities. Meanwhile, the porosity and specific surface area of spent AT(0.003)-Z500 and AT(0.005)-Z500 are comparable to those of Z500 after 12 hours of time-on-stream. These observations imply that the deactivation of the zeolite catalysts is not solely due to blockage by the traditional carbonaceous species. With the aid of ^{13}C NMR spectroscopy, other types of polymeric species were also detected. As shown in Fig. 10, ^{13}C CP-MAS NMR spectra of spent Z500 and AT(0.005)-Z500 display three typical regions. The resonance in the region between 13 and 35 ppm is attributed to the saturated carbon atoms of terminal

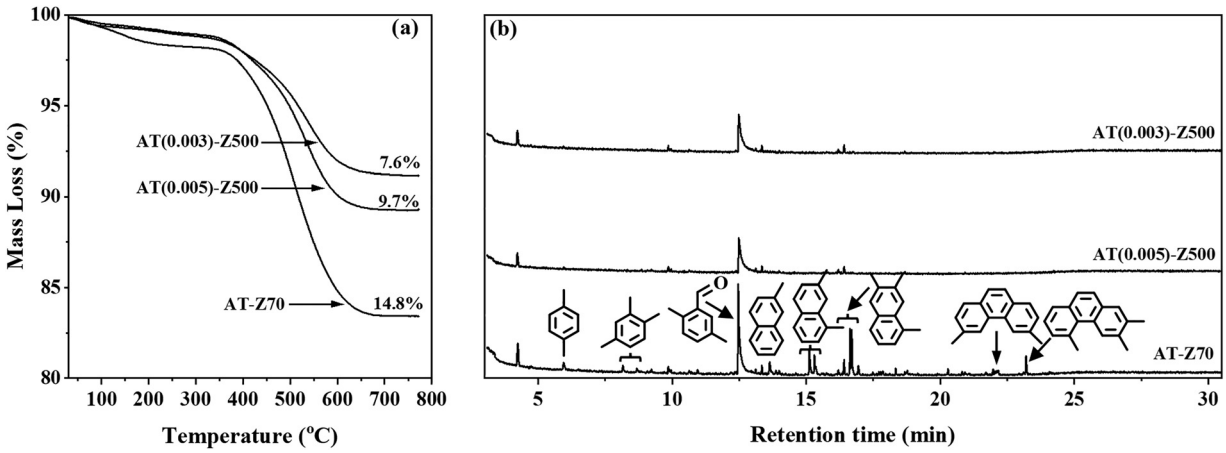

Fig. 9 Characterizations of the spent hierarchical ZSM-5 zeolites. (a) Thermal gravimetric analysis (TGA) and (b) GC-MS chromatograms of the carbonaceous species.

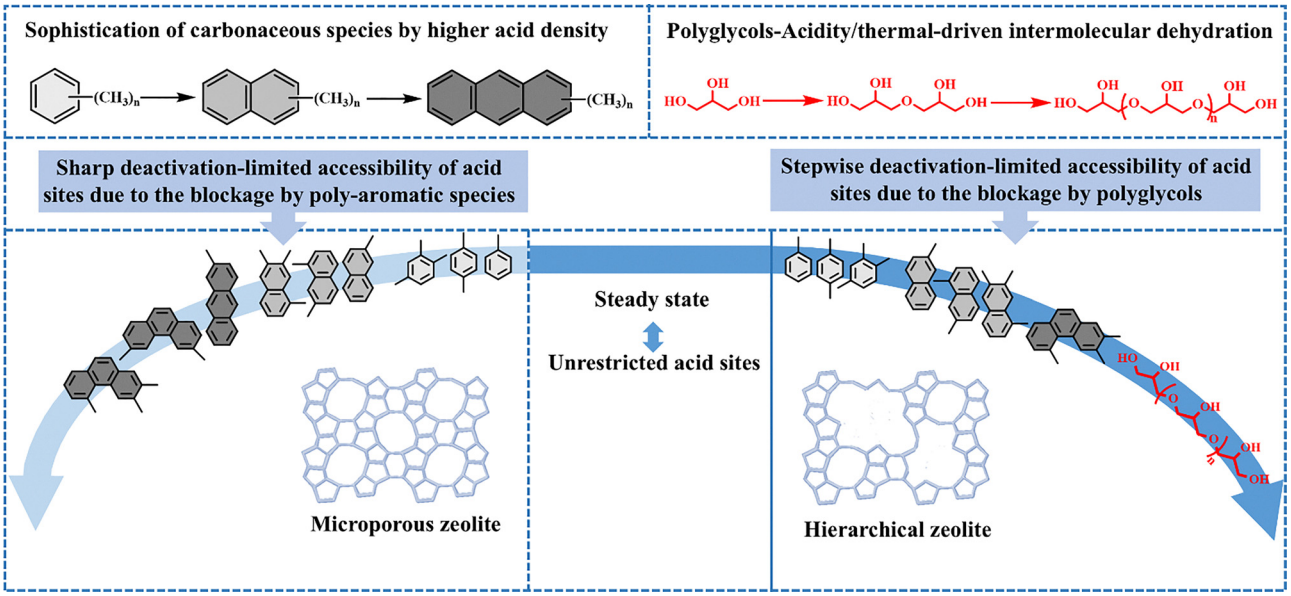

Fig. 11 Schematic of the ZSM-5 zeolite deactivation during the glycerol dehydration.

chains bound to the oligomeric species that have not yet cyclized.[39–41] The resonance in the region between 127 and 140 ppm is associated with carbon atoms in polyaromatic species.[40,42] Besides these resonances associated with common carbonaceous species, it is worth noting that the appearance of resonance in the region between 63 and 77 ppm indicates the presence of polyglycol species.[39,43,44] It is conceivable that these polyglycerol species also act like the deposited carbonaceous species, which block the zeolite pores and thereby restrict access to the acid sites. It has been reported that the intermolecular dehydration of glycerol molecules can be activated by the acid sites, which leads to the successive coupling of hydroxyl groups of glycerol for the formation of polyglycol species.[45] In fact, the resonances of polyglycol species are also clearly observed over the microporous Z500 with a poor acid site density. Therefore, the thermally induced intermolecular dehydration of glycerol molecules also imposes restrictions on the smooth running of the catalytic dehydration of glycerol by the zeolite catalysts.

In the case of catalytic dehydration of glycerol by zeolites, the accessibility of the acid sites holds priority in the reaction (Fig. 11). At the microporous level, the catalytic performance of the acid sites is constrained by their accessibility, due to blockage of the small micropore size (0.55 × 0.51 nm, 0.56 × 0.53 nm) by the carbonaceous species with sophisticated structure, the activity profiles of which are characteristic of a declining mode from the beginning, regardless of their high density within the Al-rich microporous ZSM-5. Owing to the hybridization of the mesoporous level, the acid sites at the low-density level enable a relatively smooth running of the dehydration reaction at a high conversion level (~95%) on the order of 12 hours. Although the accessibility of the acid sites is mitigated by the hierarchical porosities, the issue of stepwise deactivation remains a challenge. It should be noted that the buildup of the common carbonaceous species is not the sole impacting factor for the deactivation of the zeolite catalysts. The thermal or acid-driven intermolecular dehydration of glycerol also plays a role in the deactivation. As the reaction proceeds, the buildup of polyglycols also reduces the accessibility of the acid sites, leading to the decline in the apparent conversion of the glycerol. Such observations account for the stepwise deactivation of the hierarchical zeolites after the initial steady state.

Conclusions

In this work, the acidity and porosity of ZSM-5 zeolites are decoupled to investigate their separate roles and their interplay in the dehydration of glycerol. It can be observed that the accessibility of the acid sites has priority in determining the catalytic performance of the dehydration of glycerol. In the case of microporous ZSM-5 zeolites, the initial relatively poor conversion and the steep decline of the activity profiles are associated with the limited accessibility of the acid sites due to the dimension size constraint imposed by the micropore size of the ZSM-5 zeolite in the fresh state and the exacerbated blockage by the poly-aromatic carbonaceous species as the reaction proceeds. In such situations, the Al-rich zeolite, with high acid site density, still suffers from poor initial activity and rapid deactivation. Upon hybridization of the mesoporosity by the alkaline treatment, even the acid sites at the low-density level enable the dehydration to proceed smoothly in around 10 hours. At the hierarchical micropore-mesopore level, acid sites play multifaceted roles in the reactions: they serve as active centers for the dehydration reaction to form the target product acrolein, and simultaneously promote the formation of carbonaceous species. In particular, the enhancement of the acid site density

leads to structural sophistication of carbonaceous species to the poly-aromatics. Although the accessibility of the acid sites can be mitigated by the introduction of mesoporosity, the issue of deactivation remains an apparent challenge over the hierarchical ZSM-5 zeolites. It should be noted that the accessibility of acid sites re-emerges as the factor responsible for the deactivation over the hierarchical zeolites, which stems from blockage by the polyglycols due to the thermal or acid-driven intermolecular dehydrations. These observations enrich our fundamental understanding of the deactivation of the glycerol dehydration and are informative for the emergence of refinement strategies to address the deactivation bottlenecks.

Author contributions

Yonghua Yu: methodology, experiment, data acquisition, formal analysis, writing – original draft. Jing Niu: data acquisition and formal analysis. Dazhi Zhang: formal analysis and writing – review & editing. Shutao Xu: discussion on experiments and formal analysis. Fang Lu: discussion on experiments and formal analysis. Jiaxu Liu: formal analysis and funding acquisition. Shengjun Huang: supervision, formal analysis, writing – review & editing, conceptualization and funding acquisition.

Conflicts of interest

There are no conflicts to declare.

Data availability

The data are available upon reasonable request.

Supplementary information (SI) is available. See DOI: **https://doi.org/10.1039/d5nj03310a**.

Acknowledgements

This work was supported by the National Key Research and Development Program of China (2022YFA1504402) and the Natural Science Foundation of China (No. 21978282).

Notes and references

1 R. R. C. Monteiro, S. Arana-Peña, T. N. da Rocha, L. P. Miranda, Á. Berenguer-Murcia, P. W. Tardioli, J. C. S. dos Santos and R. Fernandez-Lafuente, *Renewable Energy*, 2021, **164**, 1566–1587.
2 S. B. Živković, M. V. Veljković, I. B. Banković-Ilić, I. M. Krstić, S. S. Konstantinović, S. B. Ilić, J. M. Avramović, O. S. Stamenković and V. B. Veljković, *Renewable Sustainable Energy Rev.*, 2017, **79**, 222–247.
3 D. Zhang, S. A. I. Barri and D. Chadwick, *Appl. Catal., A*, 2011, **400**, 148–155.
4 A. A. Farias da Costa, A. de Nazaré de Oliveira, R. Esposito, A. Auvigne, C. Len, R. Luque, R. C. Rodrigues Noronha and L. A. Santos do Nascimento, *Sustainable Energy Fuels*, 2023, **7**, 1768–1792.
5 A. L. Chun Minh, S. P. Samudrala and S. Bhattacharya, *Sustainable Energy Fuels*, 2022, **6**, 596–639.
6 D. Zhang, Q. Zhang, Z. Zhou, Z. Li, K. Meng, T. Fang, Z. You, G. Zhang, B. Yin, J. Shen, C. Yang, W. Yan and X. Jin, *ChemCatChem*, 2022, **14**, e202101316.
7 M. Eqi, Y. Yang, G. Wu, L. Li and Y. Chai, *ACS Catal.*, 2025, **15**, 5142–5154.
8 L. Omar, T. Onfroy, S. Daniele and N. Perret, *ChemCatChem*, 2023, **15**, e202201297.
9 T. Komanoya, A. Suzuki, K. Nakajima, M. Kitano, K. Kamata and M. Hara, *ChemCatChem*, 2016, **8**, 1094–1099.
10 D. Chu, H. Zhou and Z. Luo, *New J. Chem.*, 2022, **46**, 18744–18750.
11 M. Douthwaite, N. Powell, A. Taylor, G. Ford, J. M. López, B. Solsona, N. Yang, O. Sanahuja-Parejo, Q. He, D. J. Morgan, T. Garcia and S. H. Taylor, *ChemCatChem*, 2020, **12**, 3097–3107.
12 L. Huang, F. Qin, Z. Huang, Y. Zhuang, J. Ma, H. Xu and W. Shen, *ChemCatChem*, 2018, **10**, 381–386.
13 F. Fernandes Barbosa and T. Pinheiro Braga, *ChemCatChem*, 2023, **15**, e202200950.
14 W. Luo, J. Shi, T. Li, T. Wang, J. Liu, Q. Cui, Y. Tan, Y. Yue and X. Bao, *ACS Sustainable Chem. Eng.*, 2025, **13**, 321–332.
15 B. J. Vargas, C. P. Roldão, R. D. S. F. Filho, J. O. Fernandes, E. D. da Silva Ferracine, C. A. da Rosa and V. B. Mortola, *Catal. Lett.*, 2025, **155**, 328.
16 G. S. Foo, D. Wei, D. S. Sholl and C. Sievers, *ACS Catal.*, 2014, **4**, 3180–3192.
17 A. Alhanash, E. F. Kozhevnikova and I. V. Kozhevnikov, *Appl. Catal., A*, 2010, **378**, 11–18.
18 F. F. Barbosa, A. R. Loiola, S. B. C. Pergher and T. P. Braga, *Catal. Today*, 2025, **444**, 114998.
19 J. Ding, T. Ma, R. Shao, W. Xu, P. Wang, X. Song, R. Guan, K. Yeung and W. Han, *New J. Chem.*, 2018, **42**, 14271–14280.
20 Z. Wang and L. Liu, *Catal. Today*, 2021, **376**, 55–64.
21 A. Talebian-Kiakalaieh, N. A. S. Amin and Z. Y. Zakaria, *J. Ind. Eng. Chem.*, 2016, **34**, 300–312.
22 N. Pethan Rajan, S. R. Ginjupalli, S. Gadamsetti, P. Balla and V. R. Chary Komandur, *New J. Chem.*, 2024, **48**, 13715–13724.
23 K.-H. Sung and S. Cheng, *RSC Adv.*, 2017, **7**, 41880–41888.
24 B. A. Qureshi, X. Lan, M. T. Arslan and T. Wang, *Ind. Eng. Chem. Res.*, 2019, **58**, 12611–12622.
25 R. Beerthuis, L. Huang, N. R. Shiju, G. Rothenberg, W. Shen and H. Xu, *ChemCatChem*, 2018, **10**, 211–221.
26 X. Liu, L. A. O'Dell, M. Hassanpour, W. Yang, X. Zhang, Y. Sakamoto, C. Su, H. Sun, Z. Zhang and J. Huang, *ACS Sustainable Chem. Eng.*, 2025, **13**, 14388–14399.
27 T. Ma, M. Yin, C. Su, N. Guo, X. Huang, Z. Han, Y. Wang, G. Chen and Z. Yun, *J. Ind. Eng. Chem.*, 2023, **117**, 85–102.
28 Y. Yu, D. Zhang, N. Wei, K. Yang, H. Gong, C. Jin, W. Zhang and S. Huang, *Mol. Catal.*, 2020, **483**, 110768.

29 B. Ali, X. Lan, M. T. Arslan, H. Wang, S. Z. A. Gilani, S. Wang and T. Wang, *ACS Appl. Nano Mater.*, 2020, **3**, 10966–10977.
30 H. Zhang, Z. Hu, L. Huang, H. Zhang, K. Song, L. Wang, Z. Shi, J. Ma, Y. Zhuang, W. Shen, Y. Zhang, H. Xu and Y. Tang, *ACS Catal.*, 2015, **5**, 2548–2558.
31 H. P. Decolatti, B. O. Dalla Costa and C. A. Querini, *Microporous Mesoporous Mater.*, 2015, **204**, 180–189.
32 Y. T. Kim, K.-D. Jung and E. D. Park, *Microporous Mesoporous Mater.*, 2010, **131**, 28–36.
33 S.-H. Chai, H.-P. Wang, Y. Liang and B.-Q. Xu, *Green Chem.*, 2007, **9**, 1130–1136.
34 C. D. Lago, H. P. Decolatti, L. G. Tonutti, B. O. Dalla Costa and C. A. Querini, *J. Catal.*, 2018, **366**, 16–27.
35 S. Zhao, S. He, K. D. Kim, L. Wang, R. Ryoo, Z. Wang and J. Huang, *Magn. Reson. Lett.*, 2021, **1**, 71–80.
36 S. Zhao, W. D. Wang, L. Wang, W. Wang and J. Huang, *J. Catal.*, 2020, **389**, 166–175.
37 E. Tsukuda, S. Sato, R. Takahashi and T. Sodesawa, *Catal. Commun.*, 2007, **8**, 1349–1353.
38 N. Hijazi, A. Bavykina, I. Yarulina, T. Shoinkhorova, E. V. Ramos-Fernandez and J. Gascon, *Chem. Soc. Rev.*, 2025, **54**, 6335–6384.
39 B. Behera, P. Gupta and S. S. Ray, *Appl. Catal., A*, 2013, **466**, 123–130.
40 J. F. Haw, W. Song, D. M. Marcus and J. B. Nicholas, *Acc. Chem. Res.*, 2003, **36**, 317–326.
41 Y. Jiang, J. Huang, V. R. Reddy Marthala, Y. S. Ooi, J. Weitkamp and M. Hunger, *Microporous Mesoporous Mater.*, 2007, **105**, 132–139.
42 J. B. Stothers, C. T. Tan and N. K. Wilson, *Org. Magn. Reson.*, 1977, **9**, 408–413.
43 M. V. Rodrigues, C. Vignatti, T. Garetto, S. H. Pulcinelli, C. V. Santilli and L. Martins, *Appl. Catal., A*, 2015, **495**, 84–91.
44 L. H. Vieira, K. T. G. Carvalho, E. A. Urquieta-González, S. H. Pulcinelli, C. V. Santilli and L. Martins, *J. Mol. Catal. A: Chem.*, 2016, **422**, 148–157.
45 L. G. Possato, W. H. Cassinelli, T. Garetto, S. H. Pulcinelli, C. V. Santilli and L. Martins, *Appl. Catal., A*, 2015, **492**, 243–251.